# Uncertainty of the virtual image correlation method

M.L.M. François

Received: 28 January 2022 | Revised: 9 May 2022 | Accepted: 12 May 2022

DOI: 10.1002/nme.7037

RESEARCH ARTICLE

WILEY

# Uncertainty of the virtual image correlation method

**Marc Louis Maurice François**

Nantes Université, École Centrale Nantes, CNRS, GeM, UMR 6183, Nantes, F-44000, France

**Correspondence**
M. L. M. François, Faculté des Sciences et des Techniques, 2 rue de la Houssinière, BP 92208, 44322 Nantes Cedex 3, France.
Email: marc.francois@univ-nantes.fr

**Funding information**
Agence Nationale de la Recherche

**Abstract**

The virtual image correlation method applies for the measurement of silhouettes boundaries with sub-pixel uncertainty. It consists in a correlation between an image of interest and a virtual image based on a parameterized curve. It is shown that the method is exact in 1D, insensitive to contrast variation, and that the bias induced by brightness variation can be easily corrected. Optimal value of the virtual image width, the sole parameter of the method, and optimal numerical settings are established. An estimator is proposed to assess the relevance of the user-chosen parameterized curve family to match the contour. An analytical formula and a diagram are given for the measurement uncertainty in both cases of noiseless and noisy images. The results obtained are validated by tests carried out on synthetic images and on real images.

**KEYWORDS**

level sets, solids, topology design, virtual image correlation

## 1 | INTRODUCTION

The virtual image correlation (VIC) method originates from the global form of the digital image correlation (DIC) method.[1,2] However, in the VIC, the second image is an elementary and unitary virtual one which simply mimics the white to black gradient of the boundary and whose shape is defined from a parameterized curve. At convergence, when virtual and physical images are close as possible, the optimal shape parameters are obtained and the corresponding curve represents a measurement of the contour.

The most direct application of the VIC is the shape measurement. Its sub-pixel accuracy makes it applicable to metrology. In the field of mechanical measurement, DIC has established itself for the full-field measurement of displacement and deformation. However, it does not apply when the surface is too small, such as for slender objects (beams, lattices) or when the surface cannot be provided with any texture. By measuring the silhouette or contour in the initial and final states, the VIC can complement the DIC in these cases.

The very first version of the VIC was dedicated to the measurement of open contours.[3] A highly flexible fiber was measured using a curve represented by a Lagrangian series. A cantilever beam was also measured, using a beam mechanical equation, which led to an identification of its Young's modulus. The accuracy of the VIC was then successfully compared, by numerical tests, to existing ridge detection methods.[4] Another application was the tracking of a cylinder in motion in a fluid flow.[5] In this case, the curve was a circle, whose small number of shape parameters (3) allowed a high accuracy measurement (this will be demonstrated in this article). Possible applications in metrology, including comparison with caliper measurement, were presented.[6] A numerically efficient version of the VIC has been proposed, in which levelsets are used within a finite element framework.[7,8] At this occasion, NURBS were used for the measurement of silhouettes.

This was then extended in 3D for the measurement of organ shapes in medical imaging.[9] Recently, the VIC has also been used to improve the accuracy of the DIC near object boundaries.[10]

The field of mechanical measurement with the VIC and analytical equations of beams, already addressed in Reference 3, was pursued for glued beams,[11] then for inflatable beams which have specific behavior laws.[12] The first use of a finite element description in the VIC was also linked to the measurement of the deformation of inflatable beams in a wind tunnel.[13,14] On this occasion, special finite elements were used which include the appearance of folds. The mechanical properties of the coated fabric, as well as the folded areas not visible to the naked eye, were obtained by this analysis.

In a recent publication,[15] the authors propose a mechanical shape correlation (MSC) method that has similarities with the VIC. The correlation is done between a physical image and a virtual image obtained by FEM simulation and the correlation parameters are also the parameters of the mechanical model. However, in the MSC, contrary to the VIC, the physical image is not directly used for the correlation, but is replaced by an image of the distance to the object contour, obtained after binarization. This procedure certainly helps to capture large displacements but it is possible that this initial processing induces a loss of accuracy. On the contrary, the VIC uses the raw, unfiltered image. A future comparison of the performances of the two methods, in terms of accuracy, detection capacity, and computation time, will be interesting in order to specify the fields of application of each method.

For the sake of brevity, no new applications of the VIC will be presented in this article, which focuses on its accuracy. Specifically, the effect of parameterization, digital adjustments, and classical image defects on accuracy is analyzed. However, optical distortions, local variations in luminance, optical effects such as diffraction at the borders, reflections, and so forth, are not studied here from a theoretical point of view. Like any global method, the quality of the identification depends on a choice: the kinematic field for the DIC and the nature of the curve for the VIC. In this article, we propose an estimator of the capacity of the chosen curve to represent the contour of interest.

In Section 2, the main equations of the VIC are presented. Compared to previous versions of the VIC, the correlation is now calculated in the virtual image frame instead of the pixel frame, which provides simpler equations and slightly better accuracy. Section 3 is devoted to an analysis that shows the theoretical exactness of the 1D VIC and gives consequences on the influence of image brightness and contrast. In Section 4, the link between image noise and measurement uncertainty is studied. In Section 5, the uncertainties associated with the gray level discretization and with the spatial (pixel) discretization are studied. The effect of physical image blur on uncertainty is the subject of Section 6. In Section 7, the above results are merged into a single uncertainty formula and a usable chart. A procedure for analyzing the ability of the curve equation to fit the contour of interest, based on the frequency analysis of a local (unconstrained) identification, is presented in Section 8. The proposed uncertainty expressions are validated on both synthetic and real tests in Section 9. This uncertainty, already compared[4] with that of fast marching algorithm[16] and Steger's method[17] is compared in this article to two recent methods reputed for their accuracy.[18,19]

All the works presented in this article are related to the Funambule software,[20] developed by the author and freely available.

## 2 | THE VIC METHOD

### 2.1 | General expressions

The image F, which contains the silhouette of interest, represents the input data of the VIC method. Let $\mathbf{X}(X_1, X_2)$ be the position of any point in F and $F(\mathbf{X}) \in [0, 1]$ the normalized value of the gray level at this point. The silhouette is measured by looking for the best fit between F and a virtual image G that consists of a linear evolution of the gray level around a curve $\mathcal{C}$ (see Figure 1). This curve is of general equation $\mathbf{X}^c(x_1, \lambda_1, \ldots, \lambda_N)$, where $x_1 \in [0, 1]$ is the curve parameter which define the curvilinear abscissa and the $\lambda_p$ are the researched shape parameters.

Any point $\mathbf{X}$ in the vicinity of $\mathcal{C}$ can be located with respect to the curve:

$$\mathbf{X}(x_1, x_2, \lambda_1, \ldots, \lambda_N) = \mathbf{X}^c(x_1, \lambda_1, \ldots, \lambda_N) + Rx_2\ \mathbf{e}_r(x_1, \lambda_1, \ldots, \lambda_N), \tag{1}$$

where $\mathbf{e}_r$ is the local normal to the curve, $\mathbf{X}^c$ is the point closest to $\mathbf{X}$ that belongs to $\mathcal{C}$, and $Rx_2$ is the distance (in pixels) from $\mathbf{X}^c$ to $\mathbf{X}$ (see Figure 2). The virtual image is only defined for $x_2 \in [-1, 1]$, thus in a band of width $2R$ around $\mathcal{C}$. The

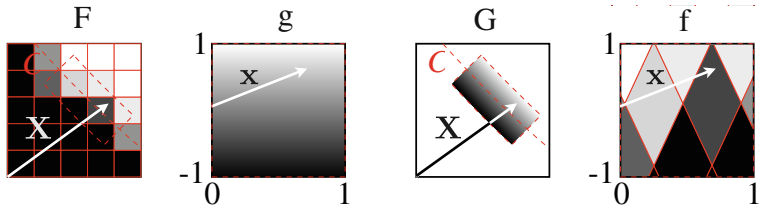


**FIGURE 1** Sketch of the VIC method

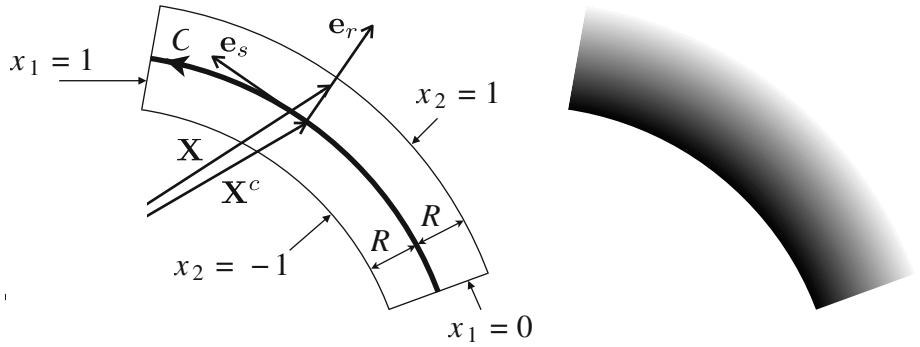


**FIGURE 2** Virtual image G geometry (left) and gray levels (right)

gray levels of G evolve linearly with respect to the distance to the curve:

$$G(\mathbf{X}) = g(\mathbf{x}), \tag{2}$$

$$g(\mathbf{x}) = \frac{1+x_2}{2}. \tag{3}$$

In the frame $\mathbf{x}(x_1, x_2)$ the image g is a simple gradient of gray along $x_2$ (Figure 1). If the method succeeded, the physical image in this frame:

$$f(\mathbf{x}) = F(\mathbf{X}) \tag{4}$$

is quite similar but is stricto sensu only defined at the pixel centers. Figure 1 shows such image f in which the red lines correspond to the pixel edges of the image F.

The goal of the method is to find the shape parameters $\lambda_p$ of $C$ for which the physical and virtual images are in best coincidence. As for many DIC methods,[1] the mean square difference between the two images is minimized. In the very first versions of the VIC,[3,4,8] this difference was computed between F and G, in the pixel frame $\mathbf{X}$. But this involves the minimization of the overall surface of the virtual image ($2RL$) thus induces a slight but unwanted line tension effect. In the present version, the difference is expressed between f and g thus in the frame $(x_1, x_2)$:

$$\Psi = \frac{\iint (f(\mathbf{x}) - g(\mathbf{x}))^2 dx_1 dx_2}{\iint dx_1 dx_2}, \tag{5}$$

where the denominator represents the area of g which is of value 2. The minimization of $\Psi$ with respect to $\lambda_p$ is achieved by using a Newton scheme, solving iteratively the $N \times N$ linear system:

$$\frac{\partial^2 \Psi}{\partial \lambda_p \partial \lambda_q} \Delta \lambda_q = -\frac{\partial \Psi}{\partial \lambda_p}, \tag{6}$$

where $\Delta\lambda_q$ is the corrector of the current values of the curve parameters $\lambda_q$ and where:

$$2\psi(\lambda_1, \dots, \lambda_N) = \int_{-1}^{1}\int_{0}^{1} (F(\mathbf{X}(x_1, x_2, \lambda_1, \dots, \lambda_N)) - g(x_2))^2 dx_1 dx_2, \tag{7}$$

$$\frac{\partial\psi}{\partial\lambda_p} = \int_{-1}^{1}\int_{0}^{1} \left(\frac{\partial F}{\partial \mathbf{X}} \cdot \frac{\partial \mathbf{X}}{\partial\lambda_p}\right)(f-g)dx_1 dx_2, \tag{8}$$

$$\frac{\partial^2\psi}{\partial\lambda_p\partial\lambda_q} = \int_{-1}^{1}\int_{0}^{1} \left[\left(\frac{\partial \mathbf{X}}{\partial\lambda_p} \cdot \frac{\partial^2 F}{\partial \mathbf{X}^2} \cdot \frac{\partial \mathbf{X}}{\partial\lambda_q} + \frac{\partial F}{\partial \mathbf{X}} \cdot \frac{\partial^2 \mathbf{X}}{\partial\lambda_p\partial\lambda_q}\right)(f-g) + \left(\frac{\partial F}{\partial \mathbf{X}} \cdot \frac{\partial \mathbf{X}}{\partial\lambda_p}\right)\left(\frac{\partial F}{\partial \mathbf{X}} \cdot \frac{\partial \mathbf{X}}{\partial\lambda_q}\right)\right] dx_1 dx_2. \tag{9}$$

Close to the solution $f \simeq g$ thus it is possible to take into account only the last term, as done in DIC.[1] In Appendix B, a study of their magnitude is detailed. Thus:

$$\frac{\partial^2\psi}{\partial\lambda_p\partial\lambda_q} \simeq \int_{-1}^{1}\int_{0}^{1} \left(\frac{\partial F}{\partial \mathbf{X}} \cdot \frac{\partial \mathbf{X}}{\partial\lambda_p}\right)\left(\frac{\partial F}{\partial \mathbf{X}} \cdot \frac{\partial \mathbf{X}}{\partial\lambda_q}\right) dx_1 dx_2, \tag{10}$$

in which, from Equation (1): the derivatives of the curve points $\mathbf{X}^c$ are either analytically or numerically known (see Appendix B for useful expressions). The tangential vector $\mathbf{e}_s$ and the normal vector $\mathbf{e}_r$ to the curve are defined as:

$$\mathbf{e}_s = \frac{\partial \mathbf{X}^c}{\partial x_1}\left\|\frac{\partial \mathbf{X}^c}{\partial x_1}\right\|^{-1}, \tag{11}$$

$$\mathbf{e}_r = \mathbf{e}_s \times \mathbf{e}_z, \tag{12}$$

where $\times$ denotes the cross product and $\mathbf{e}_z$ is the unitary vector normal to the plane. Above definition guarantees that $\mathbf{e}_r$ points uniformly outside any closed curve orientated positively. The curvilinear abscissa $s$ and the curvature $\rho$ are:

$$s = \int_{0}^{x_1} \left\|\frac{\partial \mathbf{X}^c}{\partial \xi_1}\right\| d\xi_1, \tag{13}$$

$$\rho = -\left(\frac{\partial^2 \mathbf{X}^c}{\partial x_1^2} \cdot \mathbf{e}_r\right)\left\|\frac{\partial \mathbf{X}^c}{\partial x_1}\right\|^{-2}, \tag{14}$$

and $L = s(1)$ is the overall curve length. If the non-overlapping condition:

$$|\rho|R < 1 \tag{15}$$

is not fulfilled, the center of the osculating circle of $C$ of radius $1/|\rho|$ is inside the virtual image G, thus some points in the vicinity of this center are defined at least twice. However, in a practical point of view, experience shows that it is possible to overcome this second condition as soon as the sharp corners of $C$ do not exceed the right angle because sharper angles put in coincidence inner (black) points of G with outer (white) points of F. From Equation (A1), the curve must not have any stationary points:

$$\left\|\frac{\partial \mathbf{X}^c}{\partial x_1}\right\| > 0. \tag{16}$$

Differentiating Equation (1) and using Equations (11), (12), and (14) give the differential surface element in the frame $\mathbf{X}$:

$$d\mathbf{X} = \left(\frac{\partial \mathbf{X}^c}{\partial x_1} + \rho R x_2 \left\|\frac{\partial \mathbf{X}^c}{\partial x_1}\right\| \mathbf{e}_s\right) dx_1 + R\mathbf{e}_r dx_2. \tag{17}$$

## 2.2 | Set of simplified equations in ideal cases

Close to the solution, as is the case for g (Equation 3), the gray levels of f depend mainly on $x_2$. Assuming $f(x_2)$ leads to:

$$\frac{\partial F}{\partial \mathbf{X}} = \frac{f'}{R}\mathbf{e}_r. \tag{18}$$

Together with Equation (A1), this allows the separation of variables in Equation (8):

$$\frac{\partial \psi}{\partial \lambda_p} = \frac{1}{R}\int_0^1 \frac{\partial \mathbf{X}^c}{\partial \lambda_p}\cdot \mathbf{e}_r \, dx_1 \int_{-1}^1 f'(f-g)dx_2. \tag{19}$$

The current term of the first integral is null if $\partial \mathbf{X}^c/\partial \lambda_p$ is everywhere collinear to $\mathbf{e}_s$, corresponding to a tangential motion which lets the curve unchanged: such case has to be avoided when choosing a curve equation. Thus, at convergence of the Newton scheme, when $\partial \psi/\partial \lambda_p = 0$:

$$\int_{-1}^1 f'(f-g)dx_2 = 0. \tag{20}$$

An integration by parts gives:

$$\int_{-1}^1 \left(f(x_2) - \frac{1}{2}\right) dx_2 = f^2(-1) - (1-f(1))^2. \tag{21}$$

Consequently, if the virtual image borders lie one in a white background and one in a black silhouette: $f(-1) = 0$ and $f(1) = 1$, the mean value of $f$ is $1/2$.

## 2.3 | The VIC numerical settings

The virtual image half width $R$ is the sole analytical setting of the VIC. However, the VIC uses computation points defined from a discretization of $(x_1, x_2)$ which does not correspond to the pixel grid but are spaced respectively of $\Delta x_1$ and $\Delta x_2$ such as:

$$\begin{aligned} \Delta x_1 &= \frac{1}{\text{ceil}(n_r L)}, \\ \Delta x_2 &= \frac{1}{\text{ceil}(n_r R)}, \end{aligned} \tag{22}$$

where $n_r$ is the refinement coefficient. In this way, the distance between the calculation points in the pixel grid is of the order of $1/n_r$. Such computation points are shown in blue in Figure 14. As a consequence, the gray levels of F need to be interpolated at intermediate points between the pixel centers. The type of interpolation is also a numerical setting. The influences of $R$, of $n_r$ and of the interpolation method are discussed in Section 5.

# 3 | PRELIMINARY 1D ANALYSIS

## 3.1 | Accuracy of the 1D VIC with discrete images

In this part, we consider the unidimensional VIC, taking into account the discrete nature of F and its interpolation. An ideal continuous image of a silhouette corresponds, in 1D, to a brightness $\overline{F}$ of equation:

$$\overline{F}(X_2) = (F_M - F_m)H(X_2 - X_2^0) + F_m, \tag{23}$$

where $H$ is the Heaviside distribution, $X_2^0$ the abscissa of the edge to be identified, $F_m$ the gray level of the (dark) silhouette, and $F_M$ the gray level of the (light) background. Such an image $\overline{\mathrm{F}}$ is shown by red lines in Figures 3–5 for $X_2^0 = 0.25$.

The corresponding discrete image F is obtained by assuming an ideal sensor, with a gray level proportional to the average light flux it receives and an infinite number of gray levels:

$$F(i) = \int_{i-1/2}^{i+1/2} \overline{F}(X_2) dX_2, \tag{24}$$

where $i \in \mathbb{N}$ is the pixel number. The edge of the silhouette is supposed passing by the pixel of number $i = 0$, that is, $X_2^0 \in ]-1/2, 1/2]$ thus:

$$\begin{aligned} F(i \leqslant -1) &= F_m, \\ F(0) &= \left(\frac{1}{2} + X_2^0\right) F_m + \left(\frac{1}{2} - X_2^0\right) F_M, \\ F(i \geqslant 1) &= F_M. \end{aligned} \tag{25}$$

The gray levels of these pixels are shown by blue squares in Figures 3–5.

The VIC requires the calculation of the distance between the physical and virtual images (Equation 5). In this section, we calculate it analytically, that is, in the space of real numbers, which implies to interpolate $F(X_2)$ at non-integer values of $X_2$. This corresponds to a degree of refinement $n_r \to \infty$ in Equation (22). Using a simple linear interpolation, the brightness of the interpolated image is:

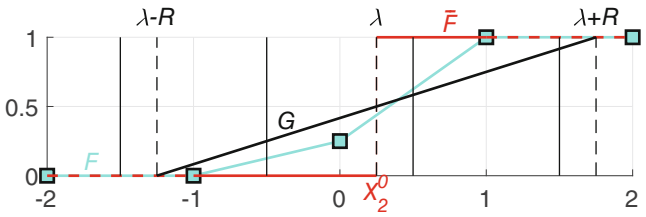


**FIGURE 3** 1D VIC with perfect image

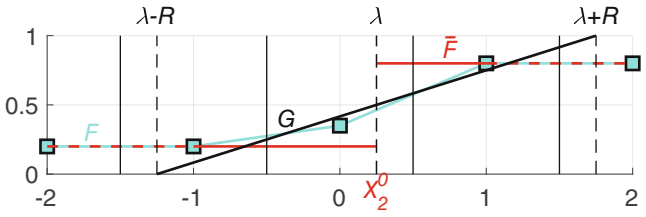


**FIGURE 4** 1D VIC with reduced contrast but no brightness bias

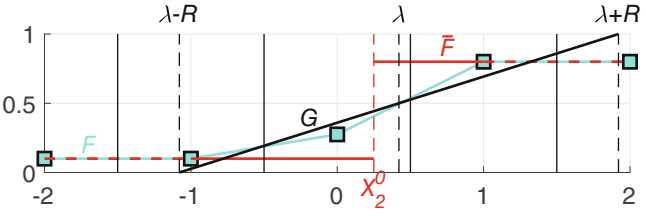


**FIGURE 5** 1D VIC with brightness bias and reduced contrast

$$
\begin{aligned}
F(X_2 < -1) &= F_m,\\
F(X_2 \in [-1, 0[) &= \left(\frac{1}{2} - X_2^0\right)(F_M - F_m)X_2 + \frac{F_M + F_m}{2} - X_2^0(F_M - F_m),\\
F(X_2 \in [0, 1[) &= \left(\frac{1}{2} + X_2^0\right)(F_M - F_m)X_2 + \frac{F_M + F_m}{2} - X_2^0(F_M - F_m),\\
F(X_2 \geqslant 1) &= F_M.
\end{aligned} \tag{26}
$$

They are represented by blue segments in Figures 3–5.

The curve $\mathcal{C}$ (Equation 1) is reduced in 1D to a point of abscissa $\lambda$, its sole shape parameter:

$$X_2 = \lambda + Rx_2. \tag{27}$$

When $\psi$ is minimum with respect to $\lambda$, Equation (21) is satisfied. If the borders of the virtual image are outside the transition pixel, its expression in the frame $X_2$ is:

$$\frac{1}{R}\int_{\lambda-R}^{\lambda+R}\left(F(X_2) - \frac{1}{2}\right)dX_2 = F_m^2 - (1 - F_M)^2. \tag{28}$$

The condition

$$R \geqslant 1.5 \tag{29}$$

guarantees that the borders of the virtual image are outside the transition pixel whatever $X_2^0$. Using Equations (26) and (28) gives:

$$\lambda = X_2^0 + R\frac{F_M(1 - F_M) - F_m(1 - F_m)}{F_M - F_m}. \tag{30}$$

This expression is much simpler once expressed with the measurement bias $\delta$ (pixel) with respect to the contrast $c$ and the brightness bias $b$:

$$\delta = \lambda - X_2^0, \tag{31}$$

$$c = F_M - F_m, \tag{32}$$

$$b = \frac{F_M + F_m - 1}{2}, \tag{33}$$

$$\delta = -2Rb. \tag{34}$$

This important result shows that the VIC is not affected by a variation of contrast but that a bias of brightness, that is, when $F_m \neq 1 - F_M$, induces a measurement bias. Figure 5 shows such case, for $R = 1.5$, $F_m = 0.8$, $F_m = 0.1$, so $c = 0.7$ and $b = -0.05$, leading to a measurement bias of $\delta = 0.15$ pixel.

Fortunately, the knowledge of the gray level of the silhouette $F_m = f(-1)$ and of that of the background $F_M = f(1)$ allow one to easily correct such brightness bias. For this, a linear correction must be used because a calculation similar to this one shows that it leads to the exact solution. In fact, the cases of Figures 3 and 4 can be seen as the case of Figure 5 with a corrected brightness. Even if the brightness is corrected, from Equation (34), it is wise to choose as small an R as possible ($R = 1.5$ in this 1D case) to limit the effect of a possible residual bias.

## 3.2 | Consequences on the 2D VIC

The previous study allows conclusions to be drawn for the actual VIC measurement, in 2D. The width of the virtual image should be as small as possible, but large enough to cover the transition zone (from background to silhouette) in all cases.

As the maximum length of a square pixel is $\sqrt{2}$, the previous relationship ($R > 1.5$ in 1D) becomes in 2D $R > 3\sqrt{2}/2$. A linear grayscale correction, so that the background is white and the silhouette is black, provides good accuracy. For this purpose, the evaluation of the current gray levels of the silhouette and the background can be done by an average:

$$F_M = \int_0^1 f(x_1, 1)dx_1, \quad F_m = \int_0^1 f(x_1, -1)dx_1. \tag{35}$$

In the previous analysis, the exact identification was obtained by making a linear interpolation of the physical pixel image. In Section 5, it will be shown that, in 2D, linear interpolation is the best among classical interpolations. Moreover, the previous results show that it is important to have a CCD sensor with good linearity.

The 2D aspects make it necessary to relativize the validity of the formula (34), in particular because of the crucial problem of the angle between the edge and the directions of the pixel grid. This will be studied in Section 5. At last, with regards to the 2D complete problem, this 1D study corresponds to a local (thus less precise) version of the VIC in which the continuity of the curve is not exploited.

## 4 | UNCERTAINTY DUE TO IMAGE NOISE

Inevitable image noise leads to uncertainty in the measurement of the VIC. We now consider that we apply the VIC on a noisy image F+E, where F is the ideal image without noise and E is an image of spatially uncorrelated Gaussian noise, with zero mean and of standard deviation $\sigma_0$. This induces a shift $\Delta\mathbf{X}^c(x_1)$ from the identified curve to the measurement without noise. Since a tangential displacement has no influence on the curve $C$, the uncertainty due to image noise is defined as the standard deviation of this shift along the normal of the curve:

$$\sigma_n^2 = \int_0^1 \sigma^2 \left(\Delta\mathbf{X}^c \cdot \mathbf{e}_r\right) dx_1. \tag{36}$$

At the first order, this deviation is associated with the variations of the parameters $\Delta\lambda_q$ by:

$$\sigma_n^2 = \sigma^2(\Delta\lambda_q) \int_0^1 \left(\frac{\partial \mathbf{X}^c}{\partial \lambda_q} \cdot \mathbf{e}_r\right)^2 dx_1. \tag{37}$$

From the Newton's scheme (Equation 6):

$$\sigma^2\left(\frac{\partial \psi}{\partial \lambda_p}\right) = \left(\frac{\partial^2 \psi}{\partial \lambda_p \partial \lambda_q}\right)^2 \sigma^2(\Delta\lambda_q). \tag{38}$$

In the case without noise case, $\partial\Psi/\partial\lambda_p = 0$ at convergence. As a consequence, in the case with noise, from Equation (8):

$$\frac{\partial \psi}{\partial \lambda_p} = \int_{-1}^1 \int_0^1 \left(\frac{\partial F}{\partial \mathbf{X}} \cdot \frac{\partial \mathbf{X}}{\partial \lambda_p}\right) \varepsilon \; dx_1 dx_2, \tag{39}$$

where $\varepsilon(x_1, x_2) = E(X_1, X_2)$ is the added image noise. In order to obtain a simple formula, we now assume that, when the identification is achieved, F and G are locally similar. From Equations (3) and (18):

$$\frac{\partial F}{\partial \mathbf{X}} = \frac{1}{2R}\mathbf{e}_r. \tag{40}$$

Supposing a weak curvature $|\rho|R \ll 1$ and, approximating from Equation (13) $\|\partial\mathbf{X}^c/\partial x_1\| = ds/d\xi_1 \simeq L$ gives:

$$dX_1 dX_2 \simeq RL dx_1 dx_2, \tag{41}$$

which shows the correspondence between the virtual image surfaces $S = 2RL$ in the frame $\mathbf{X}$ and $s = 2$ in the frame $\mathbf{x}$. From this and Equation (A1):

$$\frac{\partial \psi}{\partial \lambda_p} = \frac{1}{2R} \int_{-1}^{1} \int_{0}^{1} \left( \frac{\partial \mathbf{X}_c}{\partial \lambda_p} \cdot \mathbf{e}_r \right) \varepsilon \, dx_1 dx_2, \tag{42}$$

$$\frac{\partial^2 \psi}{\partial \lambda_p \partial \lambda_q} = \frac{1}{2R^2} \int_{0}^{1} \left( \frac{\partial \mathbf{X}^c}{\partial \lambda_p} \cdot \mathbf{e}_r \right) \left( \frac{\partial \mathbf{X}^c}{\partial \lambda_q} \cdot \mathbf{e}_r \right) dx_1. \tag{43}$$

In order to take into account the finite number of pixels, Equation (42) is transcribed in the pixel frame, thanks to Equation (41) and by considering $dX_1 = dX_2 = 1$ pixel:

$$\frac{\partial \psi}{\partial \lambda_p} = \frac{1}{2LR^2} \sum \left( \frac{\partial \mathbf{X}_c}{\partial \lambda_p} \cdot \mathbf{e}_r \right) E, \tag{44}$$

where the sum is performed on the pixels located in the band of width $2R$ of the virtual image. Consequently:

$$\sigma^2 \left( \frac{\partial \psi}{\partial \lambda_p} \right) = \frac{\sigma_0^2}{4L^2R^4} \sum \left( \frac{\partial \mathbf{X}_c}{\partial \lambda_p} \cdot \mathbf{e}_r \right)^2, \tag{45}$$

where $\sigma_0 = \sigma(E)$. Returning to the continuous virtual image frame $(x_1, x_2)$, we obtain:

$$\sigma^2 \left( \frac{\partial \psi}{\partial \lambda_p} \right) = \frac{\sigma_0^2}{2LR^3} \int_{0}^{1} \left( \frac{\partial \mathbf{X}_c}{\partial \lambda_p} \cdot \mathbf{e}_r \right)^2 dx_1. \tag{46}$$

Gathering previous results gives the researched value of $\sigma_n$. However, in order to obtain a simpler expression of the uncertainty, we will assume that $\partial^2 \psi / \partial \lambda_p \partial \lambda_q$ is a diagonal matrix:

$$\frac{\partial^2 \psi}{\partial \lambda_p \partial \lambda_q} \simeq \frac{\delta_{pq}}{2R^2} \int_{0}^{1} \left( \frac{\partial \mathbf{X}^c}{\partial \lambda_p} \cdot \mathbf{e}_r \right)^2 dx_1. \tag{47}$$

This provides a very useful and simple expression of the measurement uncertainty associated with image noise:

$$\sigma_n = \sigma_0 \sqrt{\frac{2NR}{L}}, \tag{48}$$

where $N$ is the number of shape parameters $\lambda_p$. The last hypothesis of a diagonal form of is exact if the shape parameters act on distinct segments of the $x_1$ abscissa. This is of course generally not true but, in many cases (such as B-spline curves) the shape parameters act on relatively separated domains, leading to band matrixes with strong values on the diagonal.

The proportionality between the uncertainty $\sigma_n$ and the image noise $\sigma_0$ is common with DIC uncertainty analysis.[21-24] Doubling the image resolution doubles $L$ thus divides $\sigma_n$ by $\sqrt{2}$. The uncertainty is proportional to $\sqrt{N}$: this weak dependence allows the choice of relatively complex families of curves. The smaller $R$ is, the smaller the uncertainty is, provided that the edges of the virtual image are one in the background and the other in the silhouette. Consequently, $R = 3\sqrt{2}/2$ (see Section 3), appears to be optimal.

## 5 | UNCERTAINTY DUE TO DISCRETIZATION

### 5.1 | Grayscale discretization

In real images the gray levels are transcribed into a finite number of $2^{nb}$ levels, where $nb$ is the bit depth. This loss of information is classically associated with a quantization noise:[25]

$$\sigma_{0q} = \frac{1}{2^{nb}\sqrt{12}}, \tag{49}$$

which can be taken into account in addition to the image noise $\sigma_0$. However, for real images, it is generally negligible compared to the latter.

## 5.2 | Spatial discretization

In Section 3.1, it was shown that the VIC is exact in the 1D discrete (pixel) space, whatever the position of the edge in the transition pixel. However, in 2D, the silhouette intersects the pixel grid with some angle. In particular, for small angles, staircase artifacts are a common problem in image processing.

The line segment test consists in measuring a straight edge, whose center is located at $\Delta X_{02} \in [0, 1[$ at the vertical of the image center $(X_{01}, X_{02})$ and whose angle is $\theta_0 \in [0, \pi/4]$ (see Figure 6). It mimics, at least locally, any case of VIC identification, when the curvature is negligible. The gray level of the transition pixels (those containing the edge) is calculated from the analytical ratio between the area occupied by the silhouette and the area occupied by the background.

The retained curve is a line segment whose shape parameters $\Delta X_2$ and $\theta$, are defined in the same way as the reference parameters above. Its length $L + \Delta L/\cos(\theta_0)$, which has no meaning in the physical image and thus not measurable by the VIC, is imposed. The variation of length $\Delta L \in [-0.5, 0.5]$ pixel allows to test all possible locations of the beam ends with respect to the pixel grid.

For the statistics, $\Delta X_{02}, \theta_0$ and $\Delta L$ are varied over 20 levels. Each computation is initialized at $\Delta X_2 = \alpha R$ and $\theta = \theta_0 + \alpha R/L$, where $\alpha \in [-0.5, 0.5]$ is a random number. For each test, the RMS error of the distances between the reference line and the measured segment is calculated. Due to the low dependency observed on $\Delta L$, the results are presented (at least) averaged over it.

At first we check the influence of the virtual image half-width $R$, setting $n_r = 3$, $L = 100$ (a typical value), and a linear interpolation. We observe in Figure 7 that the error grows globally with $R$. However, the error is often larger when $\theta_0 = 0$ (up to 0.01 pixel). This case seems to be similar to the 1D case (Section 3) whose analytical result is exact, but here the interpolation is done at a finite number of points whose positions influence the result. For nonzero angles, an averaging effect compensates this. This problem disappears for $R = 2$ and further integer values. Consequently, with a uniform error below 0.0032 pixels, close to the previously suggested value $3\sqrt{2}/2 \simeq 2.1$, $R = 2$ is the optimal value.

At second we check the influence of the interpolation method, setting $R = 2$, $n_r = 3$, and $L = 100$. Figure 8 shows that the simple and fast linear interpolation is the best choice. This is consistent with the analytical analysis of Section 3, but different from DIC where richer interpolations are known to give better results.[24,26,27]

At third we check the influence of the refinement $n_r$, setting $R = 2$, $L = 100$, and a linear interpolation. Because the computation time is proportional to $n_r^2$, Figure 9 shows that $n_r \simeq 3$ is clearly the best value.

Finally, the influence of the length $L$ is tested on more than two orders of magnitude for $R = 2$, $n_r = 3$, and linear interpolation (Figure 10). The empirical rule:

$$\sigma_d \simeq \frac{N}{20L}, \tag{50}$$

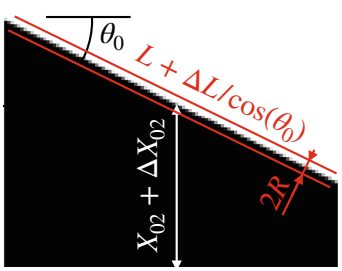


FIGURE 6 A line segment test

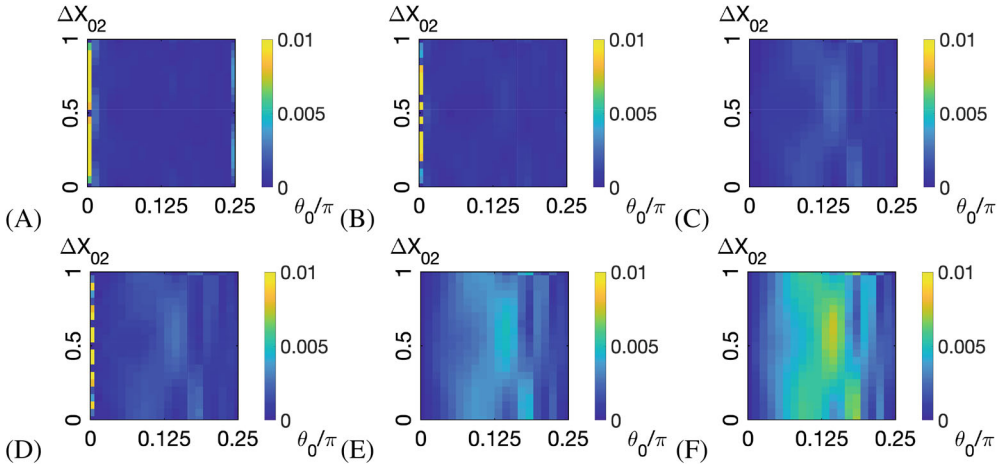


**FIGURE 7** RMS deviation (pixel) for the line segment test with (A) $R = 1$, (B) $R = \sqrt{2}$, (C) $R = 2$, (D) $R = 3\sqrt{2}/2$, (E) $R = 3$, (F) $R = 4$, in average over $\Delta L$

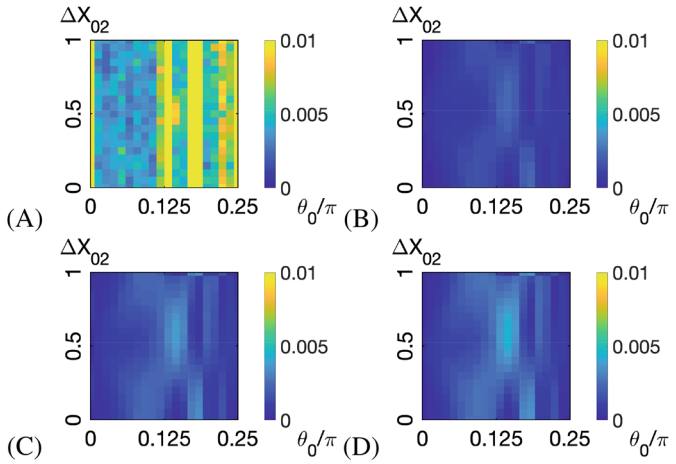


**FIGURE 8** RMS deviation (pixel) for the line segment test with interpolation method (A) nearest, (B) linear, (C) cubic, and (D) B-spline

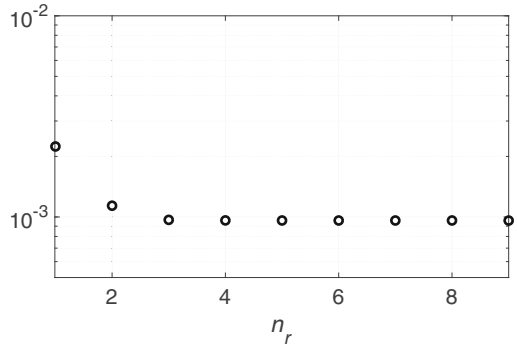


**FIGURE 9** RMS deviation (pixel) as a function of the refinement parameter $n_r$, in average over $\theta_0, X_{02}, \Delta L$

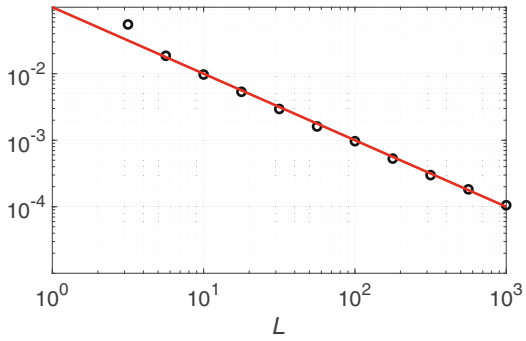


**FIGURE 10** RMS deviation (pixel) as a function of the beam length $L$, in average over $\theta_0, X_{02}, \Delta L$

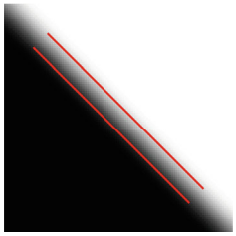

**FIGURE 11** A test with a blur of 6 pixels and $R = 4.5$ pixel

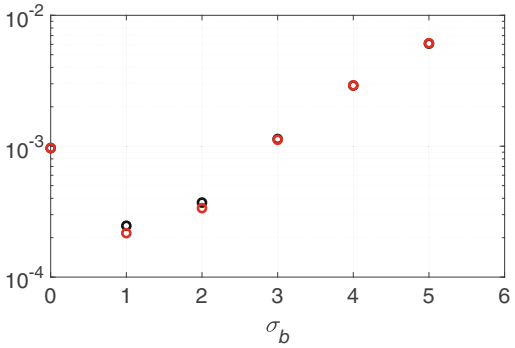


**FIGURE 12** RMS deviation (pixel) as a function of the standard deviation of the Gaussian filter, in average over $\theta_0, X_{02}, \Delta L$. Black: $R = 2$, red: $R = 2 + \sigma_b/2$

shown by the red line, is in good agreement with the tests. It supposes that the governing term is the length par number of parameters $L/N$ ($N = 2$ in these tests) because the analytical analysis of Section 4 exhibits such role of $L/N$ in Equation (48). The validity of this rule will be confirmed in Section 9.

## 6 | UNCERTAINTY DUE TO IMAGE BLUR

In order to study the influence of image blur on the accuracy, the line segment test is used by applying a Gaussian blur of standard deviation $\sigma_b$ to the image. The parameters of the VIC are fixed with a typical length $L = 100$, a refinement $n_r = 3$, and a linear interpolation but $R$ is varied. Two of the tests are shown: one with $R = 2$ and the other with $R = 2 + \sigma_b/2$, enlarged so that the virtual image better matches the blurred edge (Figure 11).

Figure 12 shows the results in average on all tests. Surprisingly enough, a moderate blur (up to $\sigma_b = 2$) improves the accuracy. We cannot conclude that the application of a (optic or digital) blur to a real image would systematically

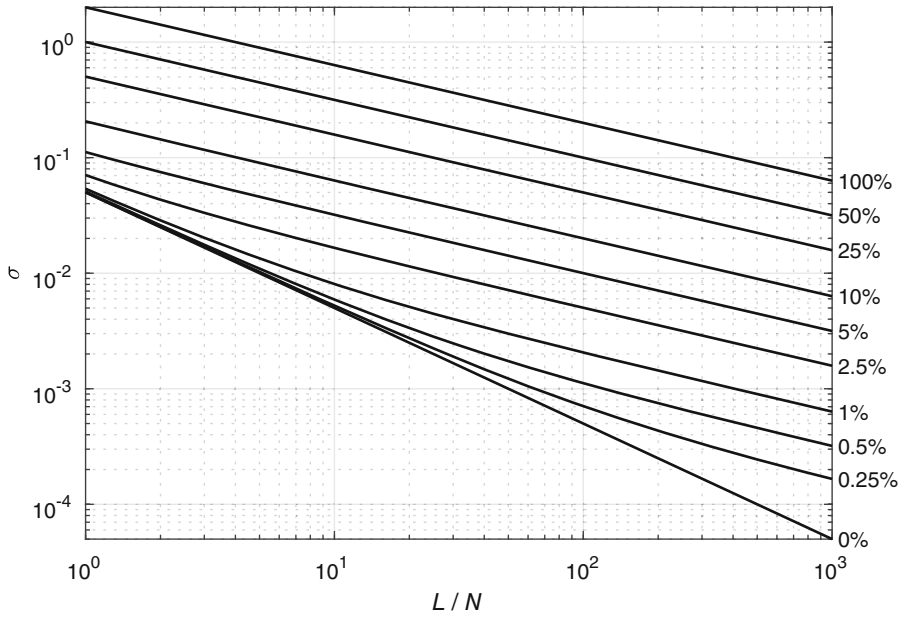


**FIGURE 13** Uncertainty of the VIC, for $R = 2$ and various image noise levels

be of benefit but it still highlights a relative insensitivity of the VIC to a moderate blur. Moreover, we observe that the enlargement of $R$ does not improve the accuracy. The fact that the virtual image is then closer to the real image seems to be compensated by the increase in uncertainty according to Equation (48).

## 7 | UNCERTAINTY FORMULA AND CHART

Assuming that (i) the chosen curve is capable of representing the contour of interest, (ii) the uncertainty associated with the noise is independent of the uncertainty associated with the discretization, and (iii) neglecting (from Section 6) the effect of (moderate) blurring, we derive the following expression for the uncertainty VIC from Equations (48) and (50):

$$\sigma^2 = 2R\sigma_0^2\frac{N}{L} + \frac{1}{400}\left(\frac{N}{L}\right)^2. \tag{51}$$

The corresponding chart shown in Figure 13 gives the uncertainty of the VIC measurement. Sub-pixel accuracy is possible even with high image noise and only a few tenths of pixels per parameter. However, accuracies better than $10^{-3}$ pixels require a few hundred pixels per parameter and low noise images. Curvature effect has been neglected in this approach but the tests in Section 9 confirm its validity in general cases. The quantization noise $\sigma_{0q}$ (Equation 49) can be taken into account within $\sigma_0$ if it is not negligible compared to the image noise.

## 8 | UNCERTAINTY DUE TO CURVE MISMATCH AND LOCAL CORRELATION INDICATOR

The remaining problem is to check whether the family of curves chosen by the user is capable of describing the contour of interest. This question is specific to global methods and also arises for DIC.[28,29] The proposed idea is to compare the result of the global VIC measurement with a local, less precise but unconstrained measurement. If the difference between these two measurements is everywhere smaller than the local measurement uncertainty, then the chosen $C$ curve family is suitable for describing the silhouette. If not, we will show that the analysis of this difference reveals the nature of the lack of flexibility of the curve family.

The local measure $\mu$ is constructed from Equation (21):

$$\mu(x_1) = \int_{-1}^{1} \left(\frac{1}{2} - f(x_1, x_2)\right) dx_2 + f^2(-1) - (1 - f(1))^2, \tag{52}$$

which is fulfilled in case of 1D measurement thus in the present case of 2D unconstrained measurement. Since the origin of $x_1$ is the (global) VIC measurement, $\mu(x_1)$ represents the distance between the VIC measurement and this local unconstrained measurement in the $(x_1, x_2)$ frame. In the pixel frame, from Equation (1), this distance is $R\mu(x_1)$. The uncertainty of this local measure is given by Equation (51) with $N = 1$ (one parameter) and $L = 1$ (one pixel):

$$\sigma^{\mu} = \sqrt{\frac{1}{400} + 2R\sigma_0^2}. \tag{53}$$

The local and global measurements are in agreement as long as $R\mu$ is less than this uncertainty. Note that the uncertainty of the VIC is negligible compared to this one because typically $N/L \simeq 100$ in Equation (51). However, the fact that the local and global measurements do not agree at a single point is not evidence that the chosen curve cannot describe the contour: this is only the case if many adjacent points are in this case. The frequency analysis of $R\mu$ gives access to this information. We will take at first an example of this analysis on the measurement of a very small disk of radius 3.333, centered at $X = 7.2345$ and $Y = 7.6789$ (pixels), in a $14 \times 14$ pixels, 16 bits image whose synthesis is described in Appendix C (see Figure 14). It is known that B-splines are not able to theoretically describe a circle.[30] If, at first sight of Figure 14, all identifications seem to fit, the same result seen in the image f frame in Figure 15 shows that the local identification $R\mu$ is in good agreement with the VIC measurement (corresponding to $Rx_2 = 0$) only for the circle. On the frequency analysis of $R\mu$ (Figure 16), we observe that all peaks are under $\sigma^{\mu}$ for the circle, showing the adequacy of this curve for this measurement. In the case of the square, the main peak of wavelength $L/4$ (the square has $N = 4$ parameters, 3 of position and its base) largely exceeds $\sigma^{\mu}$, showing that this curve is not adapted. Harmonics at higher frequencies are also visible. In the case of the B-spline, the peak at $L/4$ is the only one which exceeds, by a little, $\sigma^{\mu}$. This identification is therefore imperfect but better than the one with the square.

In actual VIC use cases, the $L/N$ ratios are of the order of 100. For this reason, the second example consists of a synthetic image (not shown) of a disk of radius 100.333 and of center (110.2345, 110.6789) (see Appendix C). Figure 17 shows FFT($R\mu$) in different cases. With a peak greater than the tolerance given by Equation (53), it is clearly indicated that the 40-side polygon (4-parameter: 2 for the center, 1 for the radius and 1 for the angle) is not suitable for this measurement. The peak at $\simeq$15 pixels is corresponding to the length of the curve divided by the number of sides of the polygon (631/40). Not surprisingly, for the B-spline, the larger the number of control points, the better the identification (up to $L/N$ is not too small). For the circle, the longest wavelengths have peaks near or below $10^{-4}$ pixels, showing the perfect relevance of the chosen curve. In any cases, peaks of magnitude of some pixels are only representative of the uncertainty of $R\mu$.

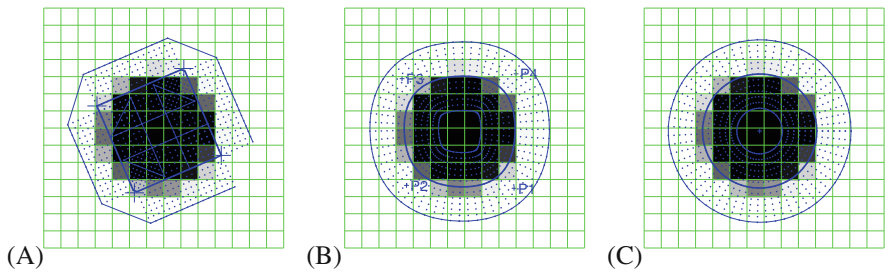


(A) (B) (C)

**FIGURE 14** Images F of the small disk and its VIC measure with: (A) Square, (B) 4-point B-spline of degree 2, and (C) circle

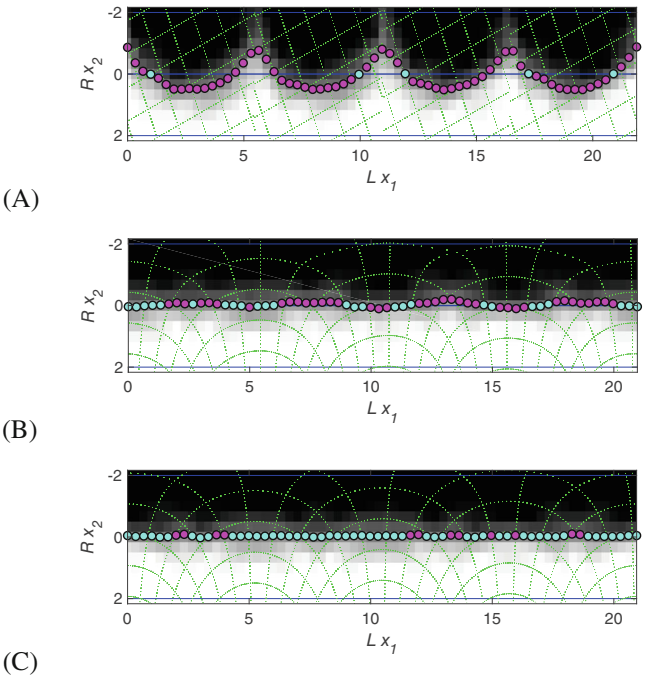


**FIGURE 15** Images f of the small disk and its VIC measure with: (A) Square, (B) 4-point B-spline of degree 2, and (C) circle. Circular marks: Local identification $R\mu$, cyan if $< \sigma^{\mu}$, magenta if $> \sigma^{\mu}$. Green dotted lines: Deformed pixel grid

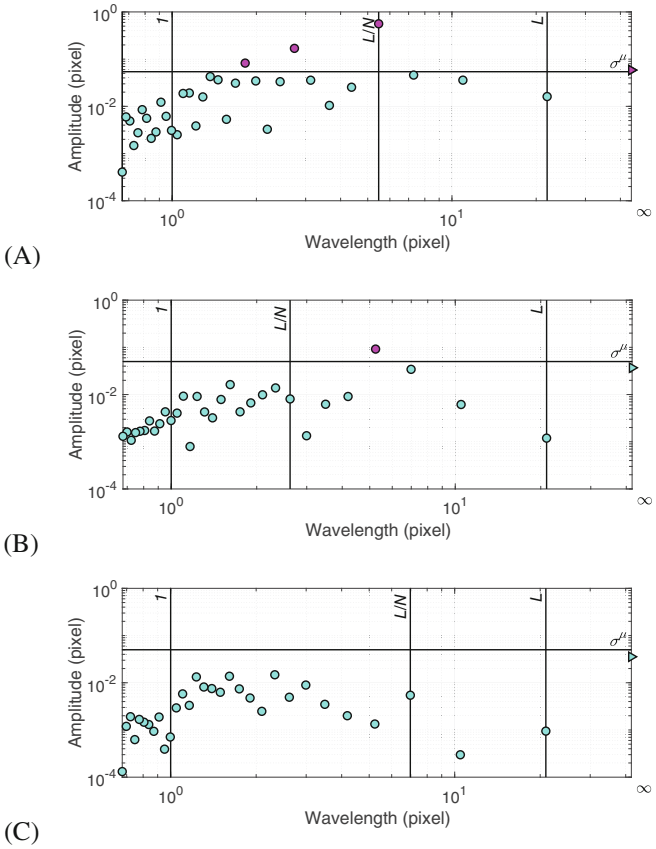


**FIGURE 16** FFT($R\mu$) for the small disk measured by: (A) Square, (B) 4-point B-spline of order 2, and (C) circle

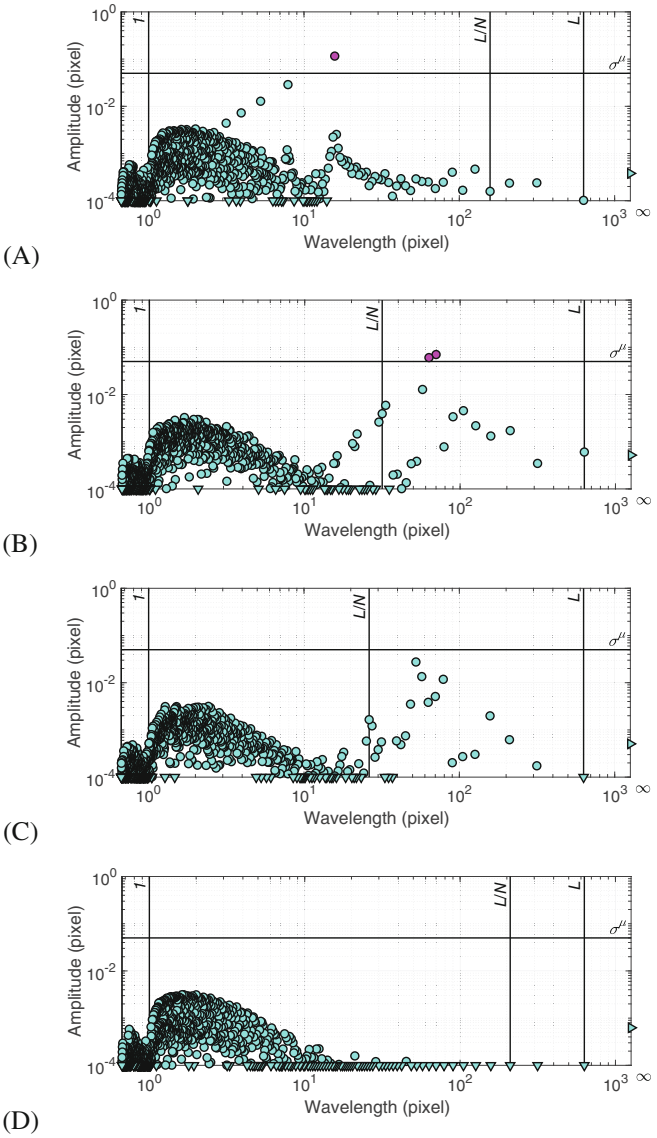


**FIGURE 17** FFT($R\mu$) for the large disk measured by: (A) 40-Side regular polygon, (B) 10-point B-spline of order 2, (C) 12-point B-spline of order 2, and (D) circle

## 9 | VALIDATION AND COMPARISON OF THE VIC UNCERTAINTY

### 9.1 | Validation of the proposed expressions on synthetic images

In Table 1, we compare predicted and measured uncertainties on various test cases. Cases $C_1$ to $C_4$, shown in Reference 4, consist in an identification of a spiral by a 10-point B-spline of order 2 in a synthetic $401 \times 401$ pixel image. Cases $D_1$ to $D_3$ refer to synthetic images of disks (see Appendix C) of average radii respectively of 3, 10, 100 pixels whose center and radius are randomly varied over 1 pixel, for 100 trials. Cases $D'_1$ to $D'_3$ are similar to them, but with an additive Gaussian image noise $\sigma_0$. All images are in 8 bits. The predicted uncertainty $\sigma$ (Equation 51) takes into account both image noise and quantization noise. The measured uncertainty $\overline{\sigma}$ consists in the standard deviation between the points measured by the VIC and the exact analytical curve which was used for the image synthesis.

One observes that the predicted uncertainties are in good agreement, although generally a bit pessimistic, with measured ones. The sole exception is the case $C_1$ for which a curve fitting error is present, the 10 control points of the

**TABLE 1** Predicted $\sigma$ and measured $\overline{\sigma}$ uncertainties on various tests

| Test case | $R$ | $L$ | $N$ | $\sigma_0$ (‰) | $\sigma_d$ (‰) | $\sigma_n$ (‰) | $\sigma$(‰) | $\overline{\sigma}$ (‰) |
|---|---|---|---|---|---|---|---|---|
| $C_1$ | 1 | 1236 | 20 | 1.1 | 0.81 | 0.20 | 0.83 | 9 |
| $C_2$ | 1 | 1236 | 20 | 300 | 0.81 | 54.0 | 54.0 | 54 |
| $C_3$ | 1 | 1236 | 20 | 500 | 0.81 | 89.9 | 89.9 | 85 |
| $C_4$ | 1 | 1236 | 20 | 900 | 0.81 | 162 | 161.9 | 180 |
| $D_1$ | 2 | 18.8 | 3 | 1.1 | 7.96 | 0.90 | 8.01 | 4 |
| $D'_1$ | 2 | 18.8 | 3 | 100 | 7.96 | 79.8 | 80.2 | 56 |
| $D_2$ | 2 | 62.8 | 3 | 1.1 | 2.39 | 0.49 | 2.44 | 0.96 |
| $D'_2$ | 2 | 62.8 | 3 | 100 | 2.39 | 43.7 | 43.8 | 30 |
| $D_3$ | 2 | 628 | 3 | 1.1 | 0.24 | 0.16 | 0.29 | 0.24 |
| $D'_3$ | 2 | 628 | 3 | 100 | 0.24 | 13.8 | 13.8 | 8 |

**TABLE 2** Measured uncertainties $\overline{\sigma}$ (‰) for active contours (AC), Trujillo–Pino's (TP), and present VIC methods

| Test case | AC | TP | VIC |
|---|---|---|---|
| $D_1$ | 44 | 6 | 4 |
| $D'_1$ | 75 | 227 | 56 |
| $D_2$ | 30 | 2.04 | 0.96 |
| $D'_2$ | 71 | 231 | 30 |
| $D_3$ | 27 | 1.95 | 0.24 |
| $D'_3$ | 69 | 236 | 8 |

B-spline being not enough to describe the spiral at this level of precision (at the time of the publication[4] no tool such as $R\mu$ was available to detect it). The C cases are related to curve measurements and not to silhouette measurements. However a curve can be seen as two silhouettes joined together and we note that the proposed estimator works in this case too.

## 9.2 | Comparison of uncertainties between VIC and local methods

The VIC has been already successfully compared to fast marching algorithm[16] and Steger's method[17] in earlier publication.[4] Since this article, new methods also claimed for sub-pixel precision. Among them we retained the work of Trujillo-Pino (TP)[18,31] which, based on an area estimate, is in some way close to the estimator $R\mu$ (Equation 52). For reference, we retained the well-known active contours (AC) method.[19] Table 2 shows the results obtained for the circular disk tests. The VIC offers better accuracy than these local methods, with an increasing gain according to the ratio $L/N$. With $L/N = 209$, tests $D_3$ and $D'_3$ are the most representative of realistic use cases. For these, the VIC was found to be 8 times more accurate than the best of the two local methods tested. For information, in the cases of the TP method with noisy images, some erroneous measurements at distance >0.5 pixel were ignored.

## 9.3 | Validation on real images

The uncertainties analyzed in this article, related to luminance and contrast defects, image noise, image discretization and curve incompatibility, are tested below in a real case. Close to the previous tests $D_1$ to $D'_3$, they consist in

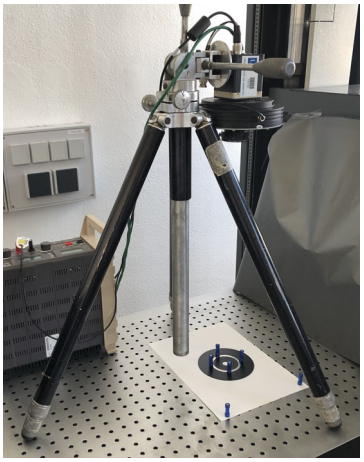

**FIGURE 18** Steel ring measurement assembly

**TABLE 3** Results of the steel ring test

| Case | Curve | Bin. | Scale (µm/pix.) | Gray lvl. (%) | Im. noise, $\sigma_0$ (%) | Avg. radius (pixel) | Meas. unc., $\overline{\sigma}$ (pixel) | Theo. unc., $\sigma$ (pixel) | Meas. unc., $\overline{\sigma}$ (µm) |
|---|---|---|---|---|---|---|---|---|---|
| $E_1$ | Ellipse | ×1 | 49.5 | [0,100] | 3.57 | 540.41 | 0.039 | 0.003 | 1.9 |
| $E_2$ | Ellipse | ×1 | 49.5 | [25,100] | 3.52 | 540.88 | 0.035 | 0.003 | 1.7 |
| $E_3$ | Ellipse | ×2 | 99 | [10,100] | 3.45 | 270.22 | 0.018 | 0.004 | 1.8 |
| $E_4$ | Ellipse | ×4 | 198 | [25,100] | 3.73 | 135.07 | 0.007 | 0.006 | 1.4 |
| $E_5$ | B.S. 8 pts | ×2 | 99 | [10,100] | 7.57 | 270.22 | 0.302 | 0.015 | 29.8 |
| $E_6$ | B.S. 12 pts | ×2 | 99 | [10,100] | 3.76 | 270.22 | 0.088 | 0.009 | 8.7 |
| $E_7$ | B.S. 20 pts | ×2 | 99 | [10,100] | 3.45 | 270.22 | 0.067 | 0.011 | 6.6 |
| $E_8$ | B.S. 32 pts | ×2 | 99 | [10,100] | 3.20 | 270.22 | 0.059 | 0.013 | 5.8 |
| $E_9$ | B.S. 48 pts | ×2 | 99 | [10,100] | 3.17 | 270.22 | 0.063 | 0.015 | 6.2 |

measuring the inner diameter of the assumed perfect circle of a camera spacer ring on which caliper measurements gave a diameter of 53.5 mm and no circularity defects. Images are taken under correct but not perfect conditions (Figure 18). In particular, time-dependent image noise was not reduced by averaging images over time, and no attention was paid to the presence of heat waves. In order to avoid problems with paint thickness and droplets, the ring has not been painted but carefully cleaned, its reflectance resulting in a white color, but also in a probable diffusion at its sharp edge. The black background is spray-painted. All equipment rests on an anti-vibration table. The camera is a 29 megapixel monochrome Imperx giving 16 bit TIFF images, the lens is a Schneider Kreuznach 50 mm Xenon Emerald chosen for its low distortion, and the lighting is a coaxial LED ring. In order to simulate an ordinary resolution image, the ring occupies only about a quarter of the image. The balance effect between image resolution and image noise suggested by Equation (51) is tested by different levels of bining. As before, the VIC measurement is performed using two mathematical curves: the ellipse which can describe a circle exactly but with excess degrees of freedom and the B-spline which cannot do so exactly (an undermatching morphing description).[30] The measurement uncertainty $\overline{\sigma}$ is calculated as the RMS deviation of the distance between the identified curve and the nearest theoretical circle. Table 3 shows the different measurements results and Figure 19 shows a case of B-spline identification.

The measure $E_1$ is realized on the full definition image with no preliminary treatment. The measured uncertainty $\overline{\sigma}$ is one order of magnitude larger than the theoretical one $\sigma$. The histogram of this image (Figure 20) presents a peak at 1, which indicates that the white of the ring is burned, and a peak close to 0.125, which corresponds to the background and

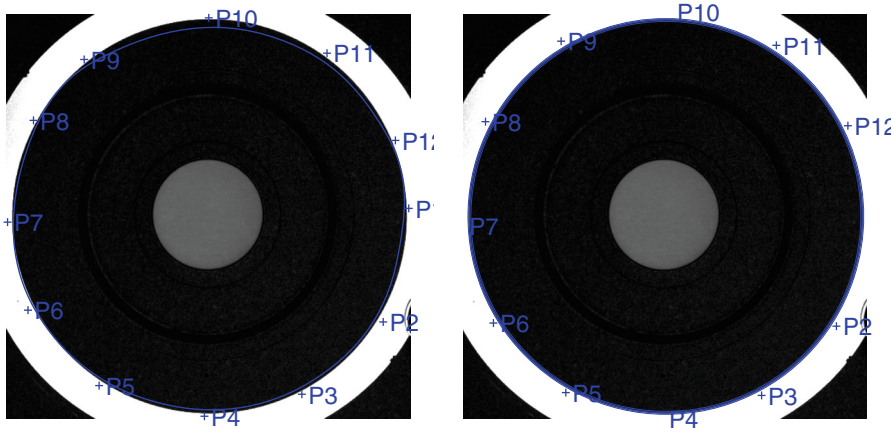


**FIGURE 19** Steel ring measure with a B-spline (case $E_6$). Left: Initial estimate. Right: Final measurement

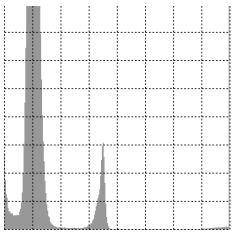

**FIGURE 20** Histogram of the image in case $E_1$

leads to an imperfect contrast and brightness. The peak at 0.45 corresponds to the central disk which is not in the definition domain of the virtual image. In order to correct this lack of contrast, the image $E_2$ was obtained from the previous image by cutting-off the gray levels below 25% and then linearly expanding them (according to the results of Section 3.1) to recover the full dynamic range. The measurement uncertainty is slightly reduced and the difference in average radii between cases $E_1$ and $E_2$ is −0.47 pixel. Setting $F_M = 1, F_m = 0.25$, and $R = 2$, formula (34) predicts a bias of −0.50 pixel which is in good agreement.

In order to test the influence of image noise and resolution, the image $E_3$ was taken with a ×2 pixel bining. At first, despite the averaging effect of the bining, the image noise is not so reduced. This suggests that the black background is not uniform, even at this scale, which can be seen in Figure 19. The experimental uncertainty is only 4.5 times larger than the theoretical uncertainty. In physical space, this leads to a measurement uncertainty (in μm) equivalent to that of the $E_2$ case, despite the half-resolution. This tendency is confirmed by an image of bining ×4 (case $E_4$) for which $\overline{\sigma}$ is (in μm) is even smaller, and very close to the theoretical uncertainty $\sigma$.

The following tests cases $E_5$ to $E_9$ are done with B-spline curves to test the local correlation indicator proposed in Section 8. The retained image is the one of the intermediate case $E_3$ and various number of control points are tested. The ratio between the measured uncertainty and the theoretical uncertainty decreases from 20 for case $E_5$ to 4.2 for case $E_9$. Only the latter value is close to the one obtained for the ellipse (case $E_3$), which suggests that the curve mismatches for cases $E_5$ to $E_8$. Furthermore, the fact that the image noise, which is calculated on $f$, is larger in the $E_5$ case also suggests a fit error due to a curve mismatch. The result of the curve matching analysis method proposed in Section 8 is shown in Figure 21. For the case $E_5$, the peak near wavelength $2L/N$ exceeds the allowable value so clearly indicates that this 8-point B-spline cannot identify the circle at this level of precision. For cases $E_6$ to $E_8$, this analysis indicates an acceptable identification but not ideal since the peak near $2L/N$ is still clearly visible. This peak only disappears completely for the 48-point B-spline which is necessary for this level of precision (case $E_9$). This study shows that the curve mismatch is revealed by the analysis of $R\mu$ as clearly as for the synthetic images (Section 8).

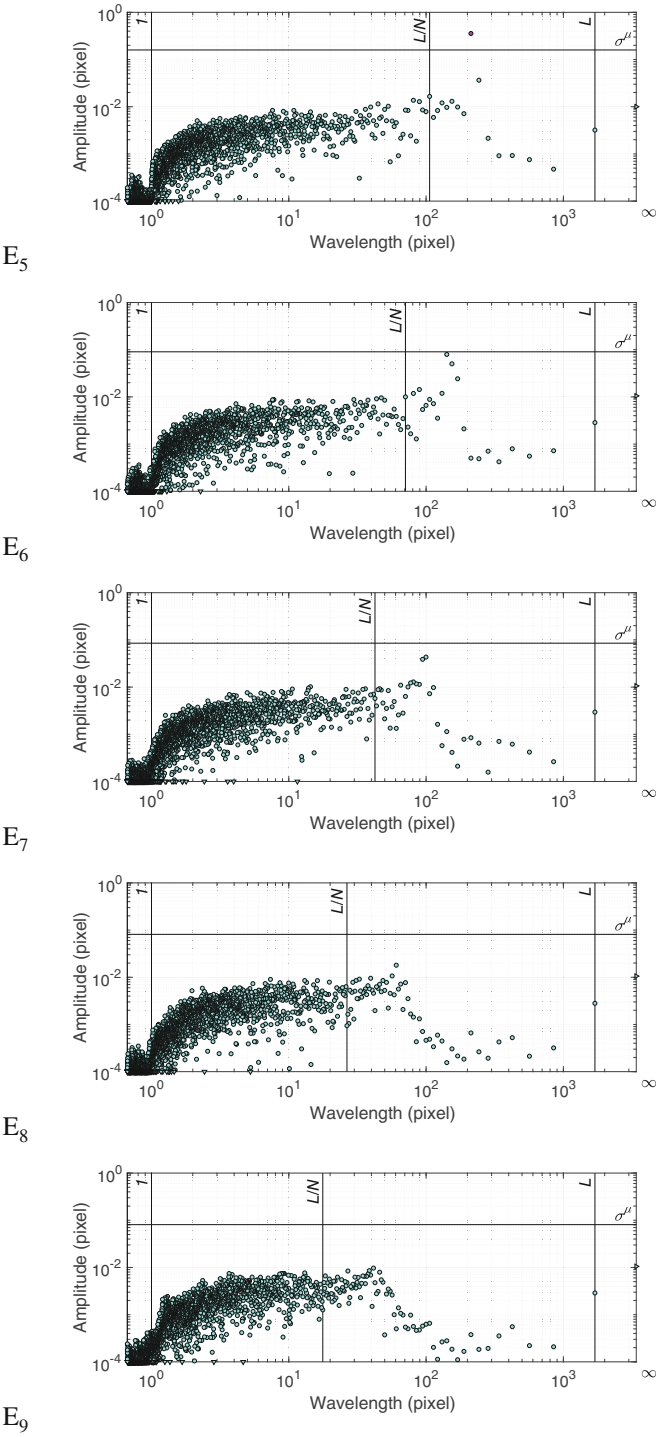


**FIGURE 21** FFT($R\mu$) for the steel ring image

## 10 | CONCLUSIONS

The VIC is now provided with an a priori value of its measurement error, with respect to the length per number of parameters and the image noise, and with an estimator of the ability of the chosen curve to represent the contour of interest. The method was shown to be insensitive to contrast variations. The measurement bias introduced by a luminance bias can be easily corrected by a linear correction. It has also been verified that a moderate blur does not affect the measurement. The optimal parameters of the method: the half-width $R$ of the virtual image, the degree of refinement $n_r$ and the type of

interpolation, are specified. However, it could be interesting to test even more sophisticated interpolation methods and more elaborate minimization functions.

The measure provided by the VIC is more accurate than the one provided by all the local methods tested. Nevertheless, the VIC still requires an initialization, that is, to start from a set of shape parameters $\lambda_p$ for which the majority of the curve points are at distance $< R$ from the boundary. This can be done by hand, or by one of the many existing contour identification methods, such as those recalled in this article.

The applications of the VIC are possible in metrology and mechanical measurement, alone or in combination with the DIC.[10] Now that other authors are doing research around the VIC,[9,15] it will be time to study the advantages and disadvantages of the different proposals.

In this article, the VIC is presented for 2D grayscale synthetic images. In case of use with color images, it will be necessary to check the influence of the Bayer filter and demosaicing on the uncertainty. The defects of the lenses (distortion, luminance inhomogeneity) have not been taken into account in this study. However, many existing tools are available to correct them. At the pixel level, the CCD sensitivity was assumed to be homogeneous and the noise Gaussian: further research is still possible in this area. The photographic technique to take a picture of a silhouette remains delicate, because of possible effects of reflection and diffraction on the edges of the physical object, of nonzero thickness. As for the DIC, the VIC will have to be equipped with adapted procedures, in particular for the preparation of surfaces and backgrounds. Further analysis of the sources of uncertainty will need to be carried out in the same way as the recent work on DIC.[29]

The 3D extension of the method[7,9] is continued, as part of the MoMaP research project, for the reconstruction of 3D images from the 2D projections of an X-ray tomography.[32] As the objects of interest are fabricated (3D lattice materials), virtual images are obtained from their CAD representation. Similar to the use of a curve for 2D VIC, this constraint improves the accuracy of the reconstruction compared to classical unconstrained methods. The work presented in this paper will need to be continued to estimate the accuracy of the 3D VIC.

## FUNDING INFORMATION

This work was granted by the French Agence Nationale de la Recherche within the MoMaP program.

## DATA AVAILABILITY STATEMENT

Data sharing is not applicable to this article as no new data were created or analyzed in this study.

## ORCID


*Marc Louis Maurice François* https://orcid.org/0000-0001-9636-3591

## REFERENCES

1. Hild F, Roux S. Digital image correlation: from displacement measurement to identification of elastic properties - A review. *Strain*. 2006;42(2):69-80.
2. Hild F, Roux S. Measuring stress intensity factors with a camera: integrated digital image correlation (I-DIC). *Comptes Rendus Mécanique*. 2006;334:8-12.
3. François MLM, Semin B, Auradou H. Identification of the shape of curvilinear beams and fibers. *Appl Mech Mater*. 2010;24-25:359-364.
4. Semin B, Auradou H, François MLM. Accurate measurement of curvilinear shapes by virtual image correlation. *Eur Phys J Appl Phys*. 2011;56:1-10.
5. Semin B, Decoene A, Hulin JP, François MLM, Auradou H. New oscillatory instability of a confined cylinder in a flow below the vortex shedding threshold. *J Fluid Mech*. 2012;690:345-365. doi:10.1017/jfm.2011.435
6. François MLM, Thomas JC, Bloch A. Métrologie de silhouettes par la méthode de corrélation d'images virtuelles. Contrôles et Mesures Optiques pour l'Industrie; 2013; SFO, Orléans, France.
7. Réthoré J, François MLM. Corrélation d'images pour la détection de contour. In: Chapelle D, Dahan M, Picart P, eds. *Actes du 20e Congrès Français de Mécanique*. Association Française de Mécanique; 2011.
8. Réthoré J, François MLM. Curve and boundaries measurement using B-splines and virtual images. *Opt Lasers Eng*. 2013;52:145-155.
9. Jiang Z, Witz JF, Lecomte-Grosbras P, et al. B-spline based multi-organ detection in magnetic resonance imaging. *Strain*. 2015;51:235-247.
10. Baconnais M, Réthoré J, François M. Improvement of the digital image correlation close to the borders of an object. *Strain*. 2020;56(3):e12340. doi:10.1111/str.12340
11. François MLM. Monitoring of debonding or cracking in bending tests by virtual image correlation. In: Chabot A, Buttlar W, Dave E, Petit C, Tebaldi G, eds. *Proceedings of the 8th International Conference on Mechanisms on Cracking and Debonding in Pavements (MCD2016)*. RILEM. Springer; 2016:739-748.

12. François MLM, Bloch A, Thomas JC. Metrology of contours by the virtual image correlation technique. In: Jin H, Yoshida S, Lamberti L, Lin M, eds. *Advancement of Optical Methods in Experimental Mechanics*. Conference Proceedings of the Society for Experimental Mechanics Series. Vol 3. Springer; 2015:239-246.
13. Bloch A, Thomas J, François M, Flamand O. Modélisation et expérimentation des structures gonflables. *Novabuild* 2014.
14. Bloch A. *Expérimentation et modélisation du comportement des structures gonflables complexes sous chargement climatique aléatoire*. PhD thesis. Université de Nantes, Nantes; 2015.
15. Kleinendorst S, Hoefnagels J, Geers M. Mechanical shape correlation: a novel integrated digital image correlation approach. *Comput Methods Appl Mech Eng*. 2019;345:983-1006. doi:10.1016/j.cma.2018.10.014
16. Sethian J. *Level Set Methods and Fast Marching Methods*. Cambridge University Press; 1998.
17. Steger C. An unbiased detector of curvilinear structures. *IEEE Trans Pattern Anal Mach Intell*. 1998;20(2):113-125.
18. Trujillo-Pino A, Krissian K, Alemán-Flores M, Santana-Cedrés D. Accurate subpixel edge location based on partial area effect. *Image Vis Comput*. 2013;31:72-90.
19. Lankton S. Active contour segmentation. https://fr.mathworks.com/matlabcentral/fileexchange/19567-active-contour-segmentation; Retrieved July 9, 2019. MATLAB Central File Exchange.
20. François MLM. Funambule; 2020. https://zenodo.org/record/3862248
21. Roux S, Hild F. Stress intensity factor measurements from digital image correlation: post-processing and integrated approaches. *Int J Fract*. 2006;140:141-157.
22. Sutton MA, Orteu JJ, Schreier HW. *Image Correlation for Shape, Motion and Deformation Measurements. Basic Concepts, Theory and Applications*. Springer; 2009.
23. Su Y, Zhang Q, Xu X, Gao Z. Quality assessment of speckle patterns for DIC by consideration of both systematic errors and random errors. *Opt Lasers Eng*. 2016;86:132-142. doi:10.1016/j.optlaseng.2016.05.019
24. Bornert M, Doumalin P, Dupré JC, et al. Assessment of digital image correlation measurement accuracy in the ultimate error regime: improved models of systematic and random errors. *Exper Mech*. 2018;58(1):33-48. doi:10.1007/s11340-017-0328-5
25. Maître H. *Du Photon Au Pixel*. ISTE; 2016.
26. Schreier HW, Braasch JR, Sutton M. Systematic errors in digital image correlation caused by intensity interpolation. *Opt Eng*. 2000;39(11):2915-2921.
27. Wang YQ, Sutton MA, Bruck HA, Schreier HW. Quantitative error assessment in pattern matching: effects of intensity pattern noise, interpolation, strain and image contrast on motion measurement. *Strain*. 2009;45(2):160-178.
28. Réthoré J. A fully integrated noise robust strategy for the identification of constitutive laws from digital images. *Int J Numer Methods Eng*. 2010;84:631-660.
29. Fayad S, Seidl D, Reu P. Spatial DIC errors due to pattern-induced bias and grey level discretization. *Exp Mech*. 2019;60:1-15. doi:10.1007/s11340-019-00553-9
30. Piegl L, Tiller W. A menagerie of rational B-spline circles. *IEEE Comput Graph Appl*. 1989;9(5):48-56.
31. Trujillo-Pino A. Accurate subpixel edge location. MATLAB central file exchange. Accessed June 28, 2019. https://www.mathworks.com/matlabcentral/fileexchange/48908-accurate-subpixel-edge-location.
32. Calmettes L, Réthoré J, François MLM. 3D metrological shape measurements from X-ray radiographs. Photomechanics iDiCs; 2021; Nantes.


**How to cite this article:** François MLM. Uncertainty of the virtual image correlation method. *Int J Numer Methods Eng*. 2022;123(18):4367-4390. doi: 10.1002/nme.7037

## APPENDIX A. USEFUL DERIVATIVES

The following derivatives of interest for the VIC are obtained from Section 2:

$$\frac{\partial \mathbf{X}}{\partial \lambda_p} = \frac{\partial \mathbf{X}^c}{\partial \lambda_p} + Rx_2 \frac{\partial \mathbf{e}_r}{\partial \lambda_p}, \tag{A1}$$

$$\frac{\partial^2 \mathbf{X}}{\partial \lambda_p \partial \lambda_q} = \frac{\partial^2 \mathbf{X}^c}{\partial \lambda_p \partial \lambda_q} + Rx_2 \frac{\partial^2 \mathbf{e}_r}{\partial \lambda_p \partial \lambda_q}, \tag{A2}$$

$$\frac{\partial}{\partial \lambda_p}\left(\left\|\frac{\partial \mathbf{X}^c}{\partial x_1}\right\|\right) = \frac{\partial^2 \mathbf{X}^c}{\partial \lambda_p \partial x_1} \cdot \mathbf{e}_s, \tag{A3}$$

$$\frac{\partial \mathbf{e}_s}{\partial x_1} = -\rho \left\|\frac{\partial \mathbf{X}^c}{\partial x_1}\right\| \mathbf{e}_r, \tag{A4}$$

$$\frac{\partial \mathbf{e}_s}{\partial \lambda_p} = \left\| \frac{\partial \mathbf{X}^c}{\partial x_1} \right\|^{-1} \left( \frac{\partial^2 \mathbf{X}^c}{\partial \lambda_p \partial x_1} \cdot \mathbf{e}_r \right) \mathbf{e}_r. \tag{A5}$$

## APPENDIX B. RELATIVE MAGNITUDE OF THE DIFFERENT TERMS IN THE MATRIX OF NEWTON'S SCHEME

The relative magnitude of the terms in Equation (9) are compared together in order to justify the use of the simplified equation (10). We suppose that, close to solution, the gray levels of F evolve, similarly to those of G, only along $\mathbf{e}_r$, thus $F(\mathbf{X}) \simeq f(x_2)$. From Appendix A and Equation (17), we have:

$$\frac{\partial F}{\partial \mathbf{X}} = \frac{f'}{R} \mathbf{e}_r, \tag{B1}$$

$$\frac{\partial^2 F}{\partial \mathbf{X}^2} = \frac{f''}{R^2} \mathbf{e}_r \otimes \mathbf{e}_r + \frac{\rho f'}{R(1+\rho R x_2)} \mathbf{e}_s \otimes \mathbf{e}_s, \tag{B2}$$

where $\otimes$ denotes the dyadic (tensor) product. For the first integral in Equation (9), supposing that the curvature radius is much larger than the virtual image width: $|\rho| R \ll 1$, gives:

$$\begin{aligned}
I_1 &= \int_{-1}^{1}\int_{0}^{1} \left( \frac{\partial \mathbf{X}}{\partial \lambda_p} \cdot \frac{\partial^2 F}{\partial \mathbf{X}^2} \cdot \frac{\partial \mathbf{X}}{\partial \lambda_q} \right) (f-g) dx_1 dx_2 \\
&\simeq \frac{1}{R} \int_0^1 \rho \left( \frac{\partial \mathbf{X}^c}{\partial \lambda_p} \cdot \mathbf{e}_s \right) \left( \frac{\partial \mathbf{X}^c}{\partial \lambda_q} \cdot \mathbf{e}_s \right) dx_1 \int_{-1}^{1} f'(f-g) dx_2 \\
&\quad - \int_0^1 \rho \left[ \left( \frac{\partial \mathbf{X}^c}{\partial \lambda_p} \cdot \mathbf{e}_s \right) \left( \frac{\partial \mathbf{e}_s}{\partial \lambda_q} \cdot \mathbf{e}_r \right) + \left( \frac{\partial \mathbf{X}^c}{\partial \lambda_q} \cdot \mathbf{e}_s \right) \left( \frac{\partial \mathbf{e}_s}{\partial \lambda_p} \cdot \mathbf{e}_r \right) \right] dx_1 \int_{-1}^{1} x_2 f'(f-g) dx_2 \\
&\quad + R \int_0^1 \rho \left( \frac{\partial \mathbf{e}_s}{\partial \lambda_p} \cdot \mathbf{e}_r \right) \left( \frac{\partial \mathbf{e}_s}{\partial \lambda_q} \cdot \mathbf{e}_r \right) dx_1 \int_{-1}^{1} x_2^2 f'(f-g) dx_2 \\
&\quad + \frac{1}{R^2} \int_0^1 \left( \frac{\partial \mathbf{X}^c}{\partial \lambda_p} \cdot \mathbf{e}_r \right) \left( \frac{\partial \mathbf{X}^c}{\partial \lambda_q} \cdot \mathbf{e}_r \right) dx_1 \int_{-1}^{1} f''(f-g) dx_2.
\end{aligned} \tag{B3}$$

Assuming further that $f$, as well as $g$, is (in average) an odd function, the integrals of $f'(f-g)$ and $x_2^2 f'(f-g)$ are zero. The function $f$ being piecewise linear (because of linear interpolation), the integral at $f''(f-g)$ is zero too. The integral in $x_2 f'(f-g)$ requires moreover that $f \simeq g$ to be small, which is reasonably true at convergence.

$$\begin{aligned}
I_2 &= \int_{-1}^{1}\int_{0}^{1} \left( \frac{\partial F}{\partial \mathbf{X}} \cdot \frac{\partial^2 \mathbf{X}}{\partial \lambda_p \partial \lambda_q} \right) (f-g) dx_1 dx_2 \\
&= \frac{1}{R} \int_0^1 \left( \frac{\partial^2 \mathbf{X}^c}{\partial \lambda_p \partial \lambda_q} \cdot \mathbf{e}_r \right) dx_1 \int_{-1}^{1} f'(f-g) dx_2 \\
&\quad - \int_0^1 \left( \frac{\partial \mathbf{e}_s}{\partial \lambda_p} \cdot \mathbf{e}_r \right) \left( \frac{\partial \mathbf{e}_s}{\partial \lambda_q} \cdot \mathbf{e}_r \right) dx_1 \int_{-1}^{1} x_2 f'(f-g) dx_2.
\end{aligned} \tag{B4}$$

Again the integral of $f'(f-g)$ is null if $f$ and $g$ are odd (or from Equation 20) but the integral of $x_2 f'(f-g)$ requires more strictly $f \simeq g$ to be small. Anyway the last integral:

$$I_3 = \int_{-1}^{1}\int_{0}^{1} \left(\frac{\partial F}{\partial \mathbf{X}} \cdot \frac{\partial \mathbf{X}}{\partial \lambda_p}\right)\left(\frac{\partial F}{\partial \mathbf{X}} \cdot \frac{\partial \mathbf{X}}{\partial \lambda_q}\right) dx_1 dx_2$$
$$\simeq \frac{1}{R^2}\int_{0}^{1} \left(\frac{\partial \mathbf{X}^c}{\partial \lambda_p} \cdot \mathbf{e}_r\right)\left(\frac{\partial \mathbf{X}^c}{\partial \lambda_q} \cdot \mathbf{e}_r\right) dx_1 \int_{-1}^{1} f'^2 dx_2, \tag{B5}$$

remains not null even when, at convergence, $f \simeq g$. It is therefore the only one kept in the expression of the second derivative of $\Psi$ in Equation (10).

## APPENDIX C. THE DISK TESTS

The images are those of a black circular disk on a white background. The gray levels of the transition pixels are obtained using a binary image (see Figure C1) of much larger definition than the desired image. A sub-pixel is black if it is inside the circle, it is white if not. The gray level of the pixel is equal to the ratio of the number of white sub-pixels to the total number of sub-pixels. The test images were calculated using a refinement factor of 1000, above which the final grayscale does not vary much more than $10^{-6}$, a precision sufficient for both 8- or 16-bit discretization and with respect to the VIC accuracy.

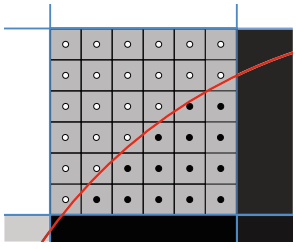

**FIGURE C1** Synthetic image computation principle